JM PAPERS

On shock-induced light-fluid-layer evolution

Yu Liang[1,2] and Xisheng Luo[2,†]

[1]NYUAD Research Institute, New York University Abu Dhabi, Abu Dhabi 129188, UAE

[2]Advanced Propulsion Laboratory, Department of Modern Mechanics, University of Science and Technology of China, Hefei 230026, PR China

Shock-induced light-fluid-layer evolution is firstly investigated experimentally and theoretically. Specifically, three quasi-one-dimensional helium gas layers with different layer thicknesses are generated to study the wave patterns and interface motions. Six quasi-two-dimensional helium gas layers with diverse layer thicknesses and amplitude combinations are created to explore the Richtmyer–Meshkov instability of a light-fluid layer. Due to the multiple reflected shocks reverberating inside a light-fluid layer, the speeds of the two interfaces gradually converge, and the layer thickness saturates eventually. A general one-dimensional theory is adopted to describe the two interfaces' motions and the layer thickness variations. It is found that, for the first interface, the end time of its phase reversal determines the influence of the reflected shocks on it. However, the reverberated shocks indeed lead to the second interface being more unstable. When the two interfaces are initially in phase, and the initial fluid layer is very thin, the two interfaces' spike heads collide and stabilise the two interfaces. Linear and nonlinear models are successfully adopted by considering the interface-coupling effect and the reverberated shocks to predict the two interfaces' perturbation growths in all regimes. The interfacial instability of a light-fluid layer is quantitatively compared with that of a heavy-fluid layer. It is concluded that the kind of waves reverberating inside a fluid layer significantly affects the fluid-layer evolution.

Key words: shock waves

1. Introduction

Richtmyer–Meshkov instability (RMI) is initiated when a shock wave impacts on an interface between two fluids with different densities (Richtmyer 1960; Meshkov 1969), and then induces finger-like flow structures such as bubbles (light fluids penetrating heavy ones) and spikes (heavy fluids penetrating light ones), and finally may cause a flow

† Email address for correspondence: xluo@ustc.edu.cn

transition to turbulent mixing. Over past decades, RMI has become a subject of intensive research due to its crucial role in various industrial and scientific fields such as inertial confinement fusion (ICF) (Lindl *et al.* 2014) and supernova explosions (Kuranz *et al.* 2018). Most previous works focused on the simple RMI case, i.e. on the semi-infinite single-mode interface evolution (Brouillette 2002; Zhou 2017*a*,*b*; Zhai *et al.* 2018), since the single mode is the fundamental component of a complex interface. However, RMI generally involves the shock-induced development of a finite-thickness fluid layer. For example, RMI occurs when the shocks generated by intense lasers or X-rays interact with the outer ablator layer, the middle push layer and the inner fuel layer of an ICF capsule. The mixing induced by RMI significantly reduces and even eliminates the thermonuclear yield. In addition, RMI occurs when the shocks generated by star collapse in a supernova interact with multi-layer heavy elements throughout interstellar space. The mixing induced by RMI shapes the filament structures in the supernova remnant. Therefore, it is significant to investigate the RMI of a finite-thickness fluid layer.

Most previous studies on the RMI of a fluid layer considered heavy-fluid-layer cases. For example, the gas curtain technique was mostly adopted to form an SF_6 fluid layer surrounded by air. It was observed that the morphologies of the shock-induced SF_6 gas layer (Jacobs *et al.* 1993; Budzinski, Benjamin & Jacobs 1994; Jacobs *et al.* 1995; Rightley, Vorobieff & Benjamin 1997) are sensitive to the initial fluid-layer shape. Late-time mixing is influenced by initial conditions, including the incident shock strength, the amplitude and wavelength of the perturbation imposed on the gas curtain, etc. (Prestridge *et al.* 2000; Balakumar *et al.* 2008; Tomkins *et al.* 2008; Orlicz *et al.* 2009; Balakumar *et al.* 2012; Orlicz, Balasubramanian & Prestridge 2013; Tomkins *et al.* 2013). Recently, the evolution of a shocked inclined SF_6 curtain was explored (Olmstead *et al.* 2017; Romero *et al.* 2021), and it was found that the pressure waves inside the heavy gas are responsible for the scale selection in fully three-dimensional initial conditions, resulting in the Kelvin–Helmholtz instability becoming dominant. Further, the soap film technique was recently utilised to generate an SF_6 gas layer with controlled perturbation and layer thickness. The heavy-fluid-layer evolution induced by a planar shock wave (Liang *et al.* 2020; Liang & Luo 2021*a*,*b*) or a cylindrical converging shock wave (Ding *et al.* 2019; Sun *et al.* 2020) was explored. It was found that rarefaction waves and compression waves reverberating inside the heavy-fluid layer result in the first interface being more unstable and the second interface being more stable (Liang & Luo 2021*a*).

Shock-induced light-fluid-layer evolution has not been well investigated yet, though it is more relevant to double-shell implosion (Montgomery *et al.* 2018; Haines *et al.* 2021). A double-shell ICF capsule consists of an outer shell (2.7 g cm^{-3}), a CH form shell (35 mg cm^{-3}) and an inner shell (200 mg cm^{-3}). The CH form shell between the other two shells is a light-fluid layer. Moreover, the reverberating waves inside a light-fluid layer are somewhat different from the waves inside a heavy-fluid layer. As a result, it is expected that the influences of the waves on the two interfaces are different under light-fluid-layer and heavy-fluid-layer conditions. Moreover, designing an appropriate layer thickness could be used advantageously to minimise mixing in an ICF capsule (Drake 2018). In this work, we utilise a shock-tube facility and the extended soap film technique to generate three quasi-one-dimensional (quasi-1-D) helium gas layers to understand the effect of the initial layer thickness on the wave patterns and interface motions, and to form six quasi-two-dimensional (quasi-2-D) helium gas layers with diverse layer thicknesses and amplitude combinations to investigate the RMI of a light-fluid layer. Linear and nonlinear theories are adopted to describe the perturbation growths at both sides of a light-fluid layer.
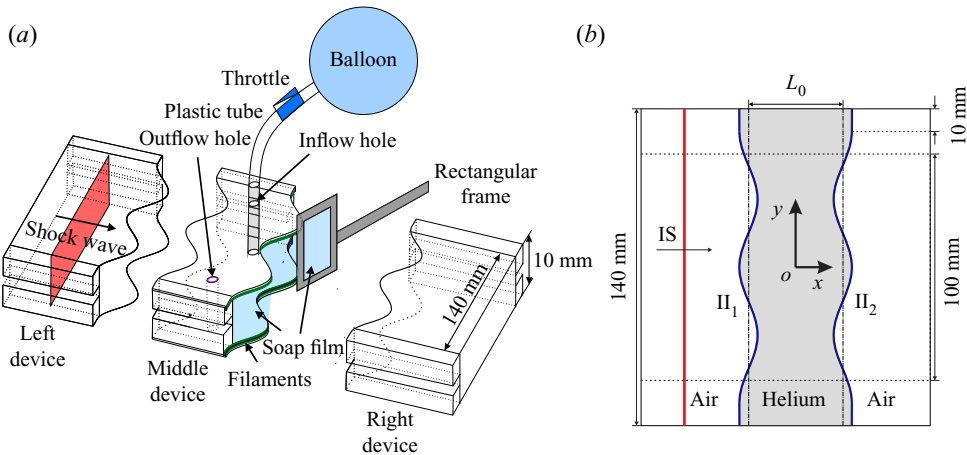
Figure 1. Schematics of (*a*) the soap film interface generation and (*b*) the initial configuration studied in the present work, where L_0 denotes the initial layer thickness; II_1 denotes the initial first interface; II_2 denotes the initial second interface; and IS denotes the incident shock wave.

The differences between the two interface perturbation growths under the light-fluid-layer and heavy-fluid-layer conditions are highlighted.

2. Experimental method

The extended soap film technique is utilised to generate two shape-controllable and discontinuous interfaces to create a helium gas layer, mainly eliminating the additional short-wavelength perturbations, diffusion layer and three-dimensionality (Liu *et al.* 2018; Liang *et al.* 2019). As shown in figure 1(*a*), three transparent devices with a width of 140.0 mm and a height of 10.0 mm are first manufactured using transparent acrylic sheets with a thickness of 3.0 mm. The adjacent boundaries of the middle device are carefully engraved to be of a sinusoidal shape with a depth of 1.8 mm. Four thin filaments (e.g. two filaments are marked green in figure 1*a*) with a height of 2.0 mm are attached to the upper and lower plates' inner surfaces at two sides of the middle device to restrict the soap film. Thus the filament bulges in the flow field with only 0.2 mm height, and its influence on the interface evolution is negligible as discussed before (Liang *et al.* 2020). Before the interface formation, the filaments are properly wetted by a soap solution with a mass fraction of 78 % distilled water, 2 % sodium oleate and 20 % glycerine. First, a small rectangular frame with moderate soap solutions dipped on its borders is pulled along the sinusoidal filaments on both sides of the middle device. Two soap film interfaces are generated, and a closed space is formed. Second, helium is pumped into the closed space through an inflow hole to discharge air inside through an outflow hole. An oxygen concentration detector is placed at the outflow hole to ensure the purity of helium inside the closed space. Subsequently, the inflow and outflow holes are sealed. Finally, the left- and right-hand transparent devices are gently connected to the middle device, and the combined one is inserted into the test section of a shock tube.

In the Cartesian coordinate system, as sketched in figure 1(*b*), the perturbations on the two interfaces are of single mode: $x = a_n^0 \cos(ky + \pi)$ within the range of $y \in [-60.0, 60.0]$ mm, where a_n^0 denotes the initial amplitude of the *n*th interface with $n = 1$ for the first interface and 2 for the second interface, and k the wavenumber of the

Case	L10-1D	L30-1D	L50-1D	L10-IP	L10-AP	L30-IP	L30-AP	L50-IP	L50-AP
a_1^0 (mm)	0	0	0	2	2	2	2	2	2
a_2^0 (mm)	0	0	0	2	−2	2	−2	2	−2
L_0 (mm)	10	30	50	10	10	30	30	50	50

Table 1. Initial physical parameters of a helium gas layer in different cases, where a_1^0 (a_2^0) represents the initial amplitude of the first (second) interface and L_0 represents the initial layer thickness.

two interfaces. In this work, $k = 104.7$ m^{-1}; a_1^0 and a_2^0 in all cases are listed in table 1. The initial layer thickness (L_0) is defined as the distance between the average positions of the initial first interface (II$_1$) and the initial second interface (II$_2$). Overall, we investigate three quasi-1-D helium gas layers with no perturbations and six quasi-2-D helium gas layers with three layer thicknesses and two amplitude combinations. Here, we define the three cases (i.e. cases L10-IP, L30-IP and L50-IP) with $a_2^0 > 0$ as in-phase cases and the three cases (i.e. cases L10-AP, L30-AP and L50-AP) with $a_2^0 < 0$ as anti-phase cases. To minimise the wall effect of the shock tube on the interface evolution, a short flat part with 10.0 mm on each side of the two interfaces is adopted. Its influence on interface evolution is negligible, as found before (Luo *et al.* 2019). The surrounding gas outside the fluid layer is air. The test gas inside the fluid layer is a mixture of helium and air, and the volume fraction of helium is 0.90 ± 0.01. Here, we define the Atwood number of a light-fluid layer (A) as $(\rho_2 - \rho_1)/(\rho_2 + \rho_1)$ with ρ_1 and ρ_2 the density of air outside the fluid layer and the density of the test gas inside the fluid layer, respectively. In this work, A equals -0.63 ± 0.01 in all cases. The ambient pressure and temperature are 101.3 kPa and 295.5 ± 1.0 K, respectively. The incident shock wave (IS) travels from left to right. The Mach number of the IS is 1.20 ± 0.01, the velocity of the IS (u_s) is 415 ± 1 m s^{-1}, the velocity of the transmitted shock (TS$_1$) inside a light-fluid layer (u_{t1}) is 883 ± 16 m s^{-1}, the jump velocity of the first interface induced by the IS (u_1^α) is 140 ± 1 m s^{-1} and the jump velocity of the second interface induced by the TS$_1$ (u_2^α) is 95 ± 1 m s^{-1}. The flow field is monitored using high-speed schlieren photography. A high-speed video camera (FASTCAM SA5, Photron Limited) is used at a frame rate of 60 000 f.p.s. and a shutter time of 1 μs. The spatial resolution of schlieren images is 0.4 mm pixel^{-1}. The flow-field visualisation is limited within the range of $y \in [-50.0, 50.0]$ mm.

3. Results and discussion

3.1. *Quasi-one-dimensional experimental results and analysis*

Schlieren images of the shock-induced quasi-1-D helium gas layer evolution are shown in figures 2(*a*)–2(*c*) for $L_0 = 10$, 30 and 50 mm, respectively. The moment when the IS impacts the average position of II$_1$ is defined as $t = 0$. Taking the L50-1D case as an example, the wave patterns and interface motions are discussed in detail. After the IS impacts the II$_1$, the reflected rarefaction waves and the TS$_1$ are generated (due to the low density of the test gas and the restricted resolution of images, it is challenging to distinguish the TS$_1$), and the shocked first interface (SI$_1$) begins to move forwards (33 μs). Then the TS$_1$ impacts the II$_2$, and the TS$_2$ moves outside the fluid layer followed by the shocked second interface (SI$_2$) (116 μs). Meanwhile, shocks are reflected and go forth and back inside the light-fluid layer since both the SI$_1$ and SI$_2$ are fast/slow interfaces relative
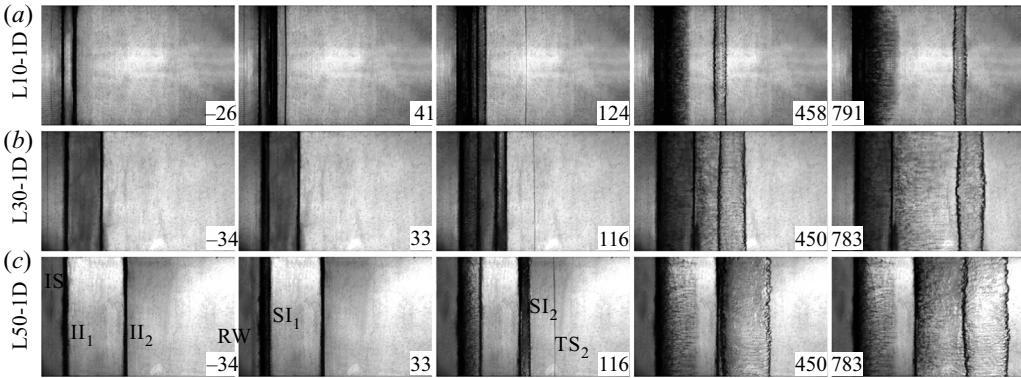
Figure 2. Schlieren images of the shock-induced quasi-1-D helium gas layer evolution in cases (*a*) L10-1D, (*b*) L30-1D and (*c*) L50-1D, where SI_1 (SI_2) denotes the shocked first (second) interface; TS_2 denotes the transmitted shock; and RW denotes rarefaction waves. Numbers indicate time in microseconds.

to the motions of the reverberated shocks. Finally, all waves refract outside the fluid layer, and the interfaces at two sides move at the same speed (783 µs).

We subtracted the background of raw experimental images, then utilised image processing software to obtain the greyscale values of the processed experimental images. Later, we acquired the coordinates of the interface contours by judging the pixels with greyscale values smaller than a specific value (generally, we chose 50). The average coordinates of an interface were obtained by calculating the average *x* coordinates at every *y* coordinate. The interface displacements (x_{SI_n}) and velocities (u_{SI_n}) of the two interfaces are measured from experiments ($n = 1$ for the first interface and $n = 2$ for the second interface), as shown in figures 3(*a*) and 3(*b*), respectively. The pixel size of schlieren images introduces the experimental measurement uncertainty. The size of error bars equals the size of symbols in figures. Time is scaled as $t u_{t1}/L_0$, interface displacement is scaled as $(x_{SI_n} - x_{01})/L_0$ with x_{01} the initial position of the first interface and interface velocity is scaled as u_{SI_n}/u_1^α. The dimensionless displacements and velocities of the first (second) interface in all L_0 cases converge, indicating that we can utilise a general 1-D theory applicable to arbitrary layer thickness to describe the motions of the two interfaces of a light-fluid layer.

The reverberated shocks and the timings when the shocks impact the two interfaces are defined in figure 4. Based on the 1-D gas dynamics theory (Drake 2018), the Mach numbers of the RF_2^α, RF_1^α, RF_2^β and RF_1^β are derived as 1.036, 1.012, 1.004 and 1.002, respectively. Although the reflected shocks are rather weak, the induced instantaneous changes in velocities of the two interfaces cannot be ignored.

The motions of the first (second) interface can be separated into three stages. Stage α: uniform motion with u_1^α (u_2^α) during $t_1^\beta > t > 0$ ($t_2^\beta > t > t_2^\alpha$); stage β: uniform motion with u_1^β (u_2^β) during $t_1^\sigma > t > t_1^\beta$ ($t_2^\sigma > t > t_2^\beta$); and stage σ: uniform motion with u_1^σ (u_2^σ) when $t > t_1^\sigma$ ($t > t_2^\sigma$). In this work, the interface velocities in all cases are derived based on the 1-D gas dynamics theory (Drake 2018) as $u_1^\beta = 111 \pm 1$ m s^{-1}, $u_1^\sigma = 107 \pm 1$ m s^{-1}, $u_2^\beta = 105 \pm 1$ m s^{-1} and $u_2^\sigma = 106 \pm 1$ m s^{-1}. Because $u_1^\sigma \approx u_2^\sigma$, it is reasonable to regard that when $t > t_2^\sigma$ all waves refract outside the light-fluid layer, and the two interfaces move
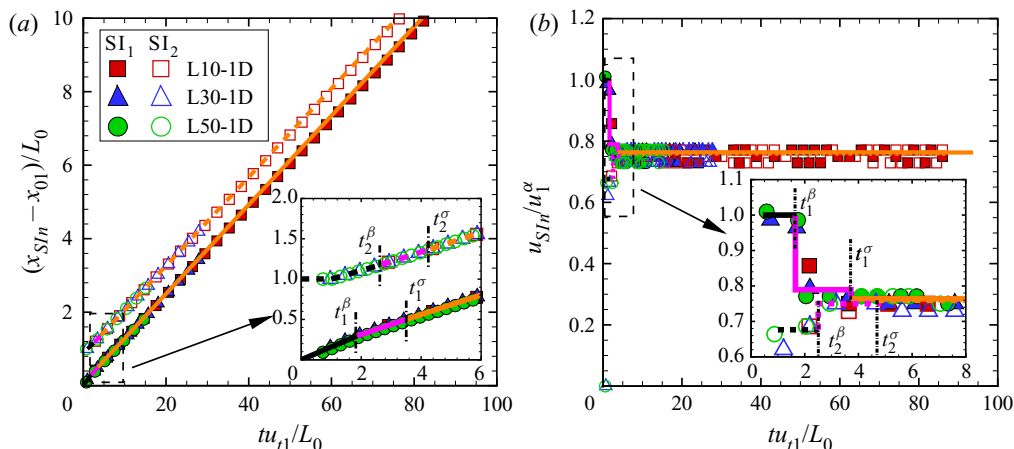
Figure 3. The dimensionless displacements (*a*) and velocities (*b*) of the first interface (filled symbols) and the second interface (open symbols). Black, purple and orange solid (dashed) lines represent the 1-D theory predictions for the first (second) interface motions in stages α, β and σ, respectively.
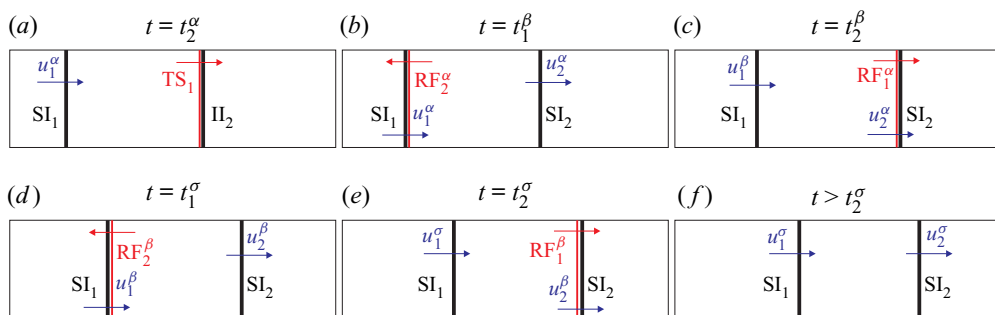

Figure 4. Sketches of (*a*) the TS$_1$ impacting II$_2$ at t_2^α, (*b*) the reflected shock (RF$_1^\alpha$) impacting SI$_1$ at t_1^β, (*c*) the reflected shock (RF$_2^\alpha$) impacting SI$_2$ at t_2^β, (*d*) the reflected shock (RF$_2^\beta$) impacting SI$_1$ at t_1^σ, (*e*) the reflected shock (RF$_1^\beta$) impacting SI$_2$ at t_2^σ and (*f*) the motions of the SI$_1$ and SI$_2$ when $t > t_2^\sigma$, where u_1^α (u_2^α), u_1^β (u_2^β) and u_1^σ (u_2^σ) are the first (second) interface velocities in stages α, β and σ, respectively.

at the same speed. The specific times t_2^α, t_1^β, t_2^β, t_1^σ and t_2^σ are separately deduced as

$$
\left.
\begin{aligned}
&t_2^\alpha = \frac{L_0}{u_{t1}}, \quad t_1^\beta = t_2^\alpha + \frac{L_0 - t_2^\alpha u_1^\alpha}{u_1^\alpha - u_{RF_2}^\alpha}, \quad t_2^\beta = t_1^\beta + \frac{L_0 - t_2^\alpha u_1^\alpha + (t_1^\beta - t_2^\alpha)(u_2^\alpha - u_1^\alpha)}{u_{RF_1}^\alpha - u_2^\alpha}, \\
&t_1^\sigma = t_2^\beta + \frac{L_0 - t_2^\alpha u_1^\alpha + (t_1^\beta - t_2^\alpha)(u_2^\alpha - u_1^\alpha) + (t_2^\beta - t_1^\beta)(u_2^\alpha - u_1^\alpha)}{u_1^\beta - u_{RF_2}^\beta}, \\
&t_2^\sigma = t_1^\sigma + \frac{L_0 - t_2^\alpha u_1^\alpha + (t_1^\beta - t_2^\alpha)(u_2^\alpha - u_1^\alpha) + (t_2^\beta - t_1^\beta)(u_2^\alpha - u_1^\beta) + (t_1^\sigma - t_2^\beta)(u_2^\beta - u_1^\beta)}{u_{RF_1}^\beta - u_2^\beta},
\end{aligned}
\right\}
$$

(3.1)

and their values are listed in table 2 for all cases. Although the specific times t_2^α, t_1^β, t_2^β, t_1^σ and t_2^σ increase as L_0 increases, the dimensionless times $t_2^\alpha u_1^\alpha / L_0$, $t_1^\beta u_1^\alpha / L_0$, $t_2^\beta u_1^\alpha / L_0$,

933 A10-6

Case	t_2^α	t_1^β	t_2^β	t_1^σ	t_2^σ	$t_2^\alpha u_1^\alpha/L_0$	$t_1^\beta u_1^\alpha/L_0$	$t_2^\beta u_1^\alpha/L_0$	$t_1^\sigma u_1^\alpha/L_0$	$t_2^\sigma u_1^\alpha/L_0$
L10-1D	11	21	31	40	49	0.16	0.30	0.43	0.55	0.68
L30-1D	34	63	91	119	146	0.16	0.30	0.43	0.55	0.68
L50-1D	57	106	152	198	244	0.16	0.30	0.43	0.55	0.68

Table 2. The specific times in the interaction of a shock wave and a helium gas layer. The unit for time is μs.
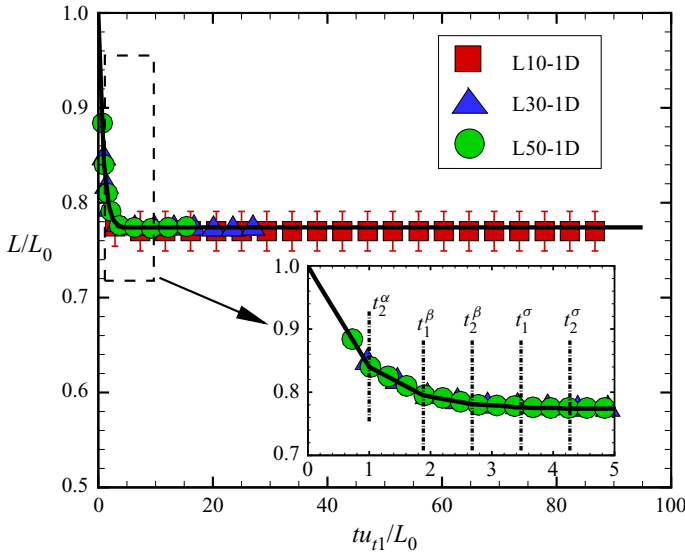

Figure 5. The time-varying dimensionless quasi-1-D helium gas layer thickness. The solid black line represents the 1-D theory prediction.

$t_1^\sigma u_1^\alpha/L_0$ and $t_2^\sigma u_1^\alpha/L_0$ are the same in different L_0 cases, indicating that the layer thickness does not influence the reflected shocks' motions. As a result, a general 1-D theory is adopted to describe the movements of the two interfaces based on the derived interface velocities and specific times in all stages. The predictions of the 1-D theory for the interface motions in stages α, β and σ are marked with black, purple and orange lines, respectively, as shown with solid lines for the first interface and dashed lines for the second interface in figure 3, and agree well with the experimental results.

The time-varying layer thickness L ($= x_{SI_2} - x_{SI_1}$) is calculated and shown in figure 5. The layer thickness is scaled as L/L_0. Before all reflected shocks refract outside the fluid layer ($t < t_2^\sigma$), L decreases gradually and finally reaches a saturated value of $0.77L_0$ in all cases. The prediction of the 1-D theory adopted in this work well agrees with the experimental data in all stages, as shown with the solid black line in figure 5.

3.2. *Quasi-two-dimensional experimental results and analysis*

Schlieren images shown in figure 6 are for shock-induced quasi-2-D helium gas layer evolution. Taking the L50-AP case as an example, the deformations of the two interfaces are discussed in detail. After the IS impacts the perturbed II_1, the rippled rarefaction waves
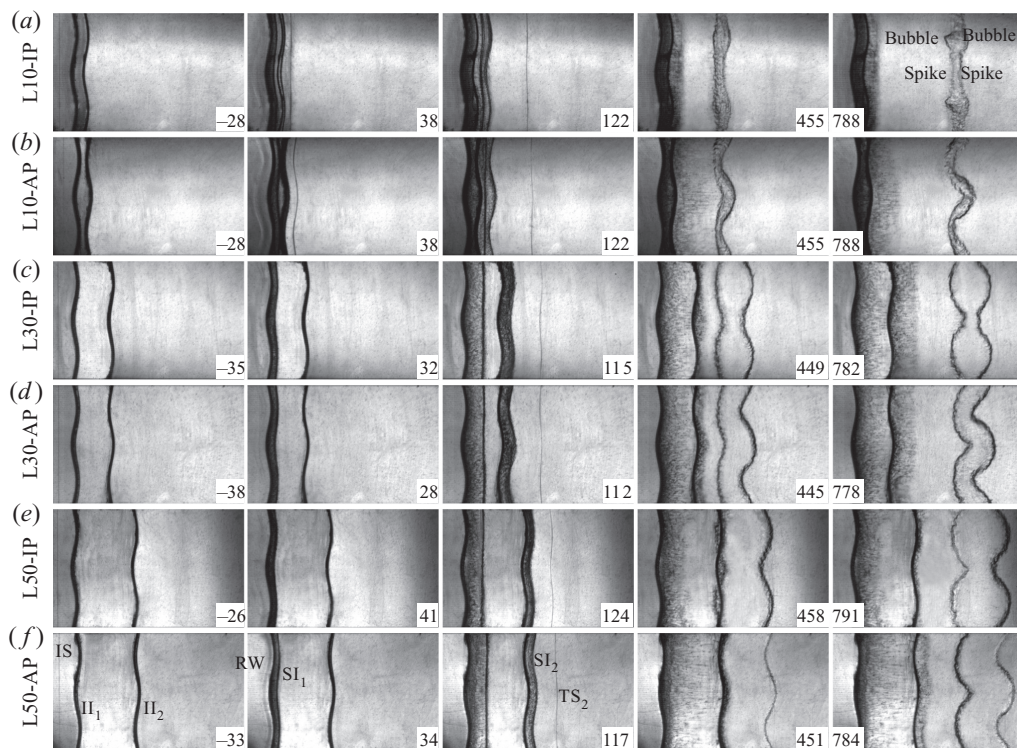
Figure 6. Schlieren images of the shock-induced quasi-2-D helium gas layer evolution in cases (*a*) L10-IP, (*b*) L10-AP, (*c*) L30-IP, (*d*) L30-AP, (*e*) L50-IP and (*f*) L50-AP. Numbers denote time in microseconds.

are reflected outside the fluid layer and the rippled TS_1 moves towards the II_2 (34 μs). Meanwhile, the perturbation on the SI_1 decreases due to the phase-reversal process (Brouillette 2002). After the TS_1 impacts the perturbed II_2, the rippled TS_2 moves outside the fluid layer, and the perturbation on the SI_2 gradually increases (117 μs). Meanwhile, the perturbation on the SI_1 reduces to zero, indicating the end of the phase-reversal process. Later, the perturbation on the SI_1 gradually increases (451 μs), and finally the two interfaces evolve similarly (784 μs). Under the light-fluid-layer condition, the final phase of the SI_2 in the three in-phase cases is the opposite to that of the SI_1, whereas the final phase of the SI_2 in the three anti-phase cases is the same as that of the SI_1. This observation is the same as for a heavy-fluid-layer counterpart (Liang *et al.* 2020; Liang & Luo 2021*a*). Especially, contrary to the general knowledge of a classical single-mode interface that the spike is sharp and the bubble is flat, the spike of the SI_1 is flat and the bubble of the SI_1 is sharp in the L10-IP case. In addition, the spike heads of two interfaces almost collide with each other in the L10-IP case at a later time (788 μs).

The amplitudes of the first and second interfaces, a_1 and a_2, are defined as half of the streamwise distance between the spike head and the bubble head of the first and second interfaces, respectively. The time-varying amplitudes of the two interfaces are measured from experiments and shown in figure 7. For the first interface, the amplitude is scaled as $\eta_1 = k(|a_1| - |Z_1 a_1^0|)$ with a compression factor Z_1 ($= 1 - u_1^\alpha/u_s$) of 0.66 in all cases; and time is scaled as $\tau_1 = k|v_1^{MB}|t$, in which v_1^{MB} is the linear amplitude growth rate calculated
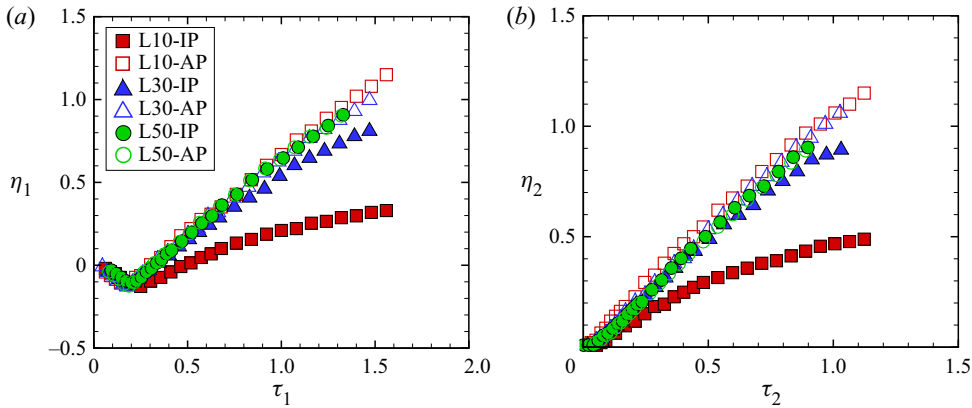
933 A10-8

Figure 7. Comparisons of the dimensionless amplitudes of the first interface (*a*) and the second interface (*b*) in all cases.

with the modified impulsive theory (Meyer & Blewett 1972):

$$v_1^{MB} = \frac{(Z_1 + 1)a_1^0 A u_1^\alpha}{2}. \tag{3.2}$$

In this work, v_1^{MB} equals -15.4 m s^{-1} in all cases. For the second interface, the amplitude is scaled as $\eta_2 = k(|a_2| - |Z_2 a_2^0|)$ with a compression factor Z_2 ($= 1 - u_2^\alpha/u_{t1}$) of 0.89 in all cases; and time is scaled as $\tau_2 = k|v_2^R|(t - t_2^\alpha)$, in which v_2^R is the linear amplitude growth rate calculated with the impulsive theory (Richtmyer 1960):

$$v_2^R = Z_2 a_2^0 A u_2^\alpha. \tag{3.3}$$

In this work, v_2^R equals 11.2 m s^{-1} in the three in-phase cases and -11.2 m s^{-1} in the three anti-phase cases. In the three in-phase cases, as L_0 decreases, both the dimensionless a_1 and a_2 decrease. On the contrary, in the three anti-phase cases, as L_0 decreases, both the dimensionless a_1 and a_2 increase. Moreover, except for the large L_0 cases (i.e. cases L50-IP and L50-AP), the dimensionless a_1 and a_2 in the anti-phase cases are larger than those in the corresponding in-phase cases with the same L_0, which is ascribed to the interface-coupling effect on the RMI of a fluid layer (Jacobs *et al.* 1995; Mikaelian 1996; Liang *et al.* 2020; Liang & Luo 2021*a*). It is concluded that a light-fluid layer consisting of two initially anti-phase interfaces is more unstable than a light-fluid layer consisting of two initially in-phase interfaces and a semi-infinite single-mode interface, especially when the initial fluid layer is thin.

According to the above analysis of the shock-induced quasi-1-D helium gas layer evolution, the growths of a_1 and a_2 are separated into three stages. First of all, in stage α, the vorticity deposition induced by the IS (TS$_1$) on the first (second) interface dominates the RMI of the first (second) interface. Jacobs *et al.* (1995) introduced linear solutions (J model) for describing the amplitude growth rates of the first interface (v_1^α) and the second interface (v_2^α) of a thin SF$_6$ gas curtain with a jump velocity of Δu imposed by a shock

wave as

$$
\left.\begin{aligned}
v_1^\alpha &= \frac{k\Delta u \left[A_t(a_1^0 - a_2^0) + A_c(a_1^0 + a_2^0)\right]}{2}, \\
v_2^\alpha &= \frac{k\Delta u \left[A_t(a_1^0 - a_2^0) - A_c(a_1^0 + a_2^0)\right]}{2},
\end{aligned}\right\}
\tag{3.4}
$$

with two modified Atwood numbers:

$$
A_t = \frac{\rho_2 - \rho_1}{\rho_2 \tanh(kL_0/2) + \rho_1} \quad \text{and} \quad A_c = \frac{\rho_2 - \rho_1}{\rho_2 \coth(kL_0/2) + \rho_1}.
\tag{3.5a,b}
$$

When $L_0 \to \infty$, $A_t = A_c = A$ and the J model reduces to the impulsive theory (Richtmyer 1960). Unlike the impulsive theory, the J model adopts the pre-shock parameters and ignores the shock compression effect. Also, for the first interface, both pre- and post-shock parameters should be considered (Meyer & Blewett 1972) since the first interface is a slow/fast one relative to the motion of the IS. Different from a thin SF_6 gas curtain investigated by Jacobs *et al.* (1995), the jump velocities of the two interfaces of a light-fluid layer (i.e. u_1^α and u_2^α) are somewhat different. Here, we modify the J model for the first interface according to the modified impulsive theory (Meyer & Blewett 1972) and the second interface based on the impulsive theory (Richtmyer 1960). Then the modified J model (mJ model) considering different jump velocities for the two interfaces is expressed as

$$
\left.\begin{aligned}
v_1^\alpha &= \frac{ku_1^\alpha \left\{A_t\left[(Z_1 + 1)a_1^0/2 - Z_2a_2^0\right] + A_c\left[(Z_1 + 1)a_1^0/2 + Z_2a_2^0\right]\right\}}{2}, \\
v_2^\alpha &= \frac{ku_2^\alpha \left\{A_t\left[(Z_1 + 1)a_1^0/2 - Z_2a_2^0\right] - A_c\left[(Z_1 + 1)a_1^0/2 + Z_2a_2^0\right]\right\}}{2},
\end{aligned}\right\}
\tag{3.6}
$$

with two new modified Atwood numbers:

$$
A_t = \frac{\rho_2 - \rho_1}{\rho_2 \tanh(Z_L kL_0/2) + \rho_1} \quad \text{and} \quad A_c = \frac{\rho_2 - \rho_1}{\rho_2 \coth(Z_L kL_0/2) + \rho_1},
\tag{3.7a,b}
$$

where a new compression factor $Z_L = 1 - u_1^\alpha/v_{t1}$ is introduced considering the compression of the shock wave on the layer thickness, and it equals 0.84 in all cases. The values of A_t, A_c, v_1^α and v_2^α are listed in table 3. In cases L50-IP and L50-AP, $A_t = A_c = A$, indicating the interface-coupling effect has a limited influence on the RMI of a light-fluid layer when $kL_0 \geqslant 5.24$. As L_0 decreases, the discrepancy between A_t and A_c increases, and, therefore, the interface-coupling effect on RMI is more and more prominent. The predictions of the mJ model are shown with solid black lines for the first interface and dashed black lines for the second interface in figure 8 for all cases, and one can find that the predictions agree well with the experimental results in stage α.

In stage β, the RF_2^α (RF_1^α) deposits additional vorticity on the first (second) interface, leading to the primary post-reshock amplitude growth rate of the first (second) interface, i.e. v_1^β (v_2^β), different from v_1^α (v_2^α). For the first interface, since it experiences a phase-reversal process early, its phase when the RF_2^α impacts it decides the effect of the RF_2^α on its instability. The end time of the first interface's phase reversal (t_1^{rev}) can be
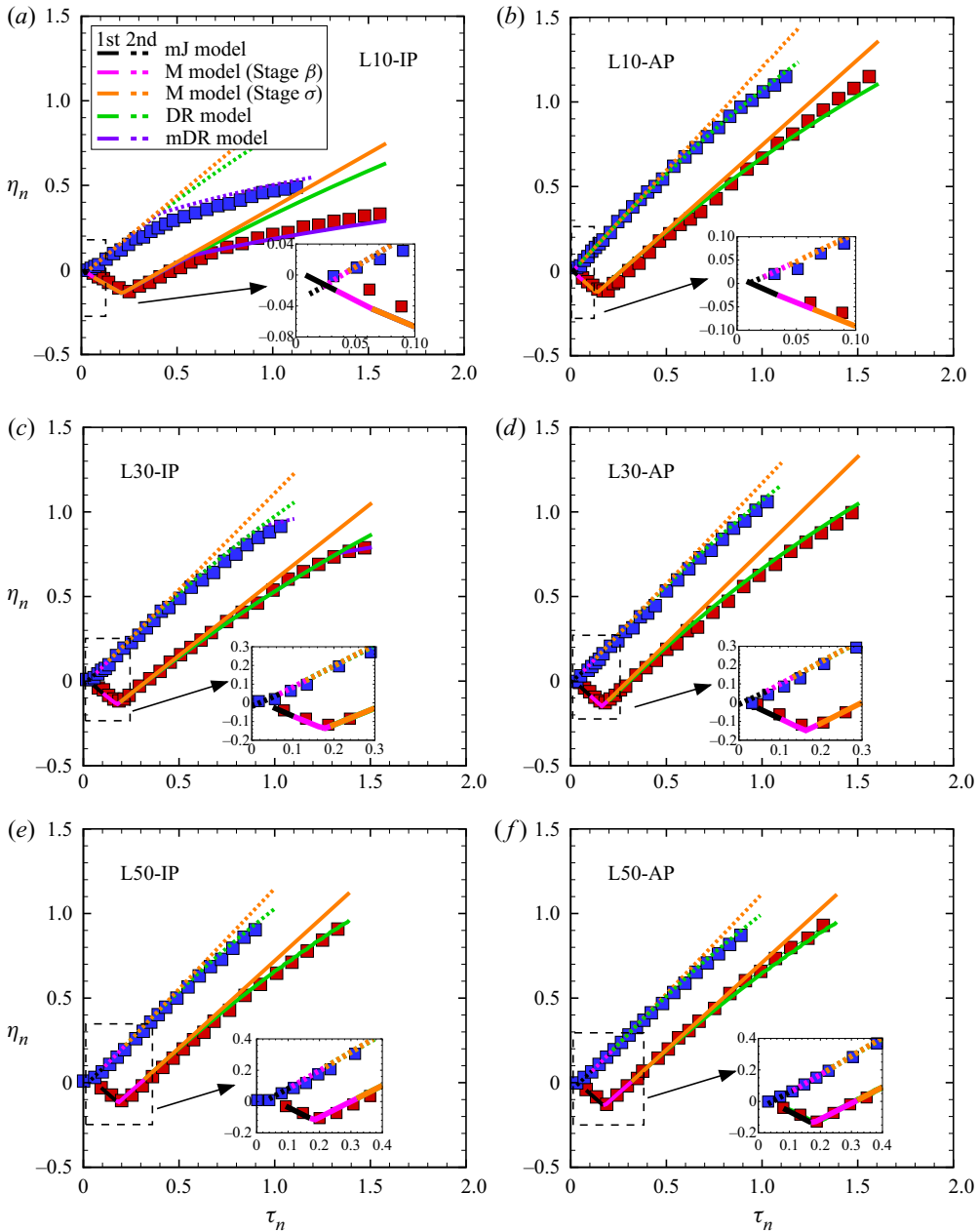
933 A10-10

Figure 8. Comparisons of the amplitudes of the first interface (red symbols) and the second interface (blue symbols) measured from experiments with theories in cases (*a*) L10-IP, (*b*) L10-AP, (*c*) L30-IP, (*d*) L30-AP, (*e*) L50-IP and (*f*) L50-AP. The solid (dashed) black lines represent the predictions of the mJ model in stage α for the first (second) interface amplitudes. The solid (dashed) light purple lines represent the predictions of the M model in stage β for the first (second) interface amplitudes. The solid (dashed) orange, green and dark purple lines represent the predictions of the M model, DR model and mDR model in stage σ for the first (second) interface amplitudes, respectively. Here $n = 1$ for the first interface and $n = 2$ for the second interface, and similarly hereinafter.

Case	L10-IP	L10-AP	L30-IP	L30-AP	L50-IP	L50-AP
A_t	−0.71	−0.71	−0.65	−0.65	−0.63	−0.63
A_c	−0.50	−0.50	−0.61	−0.61	−0.63	−0.63
v_1^α	−12.0	−17.4	−14.9	−15.8	−15.3	−15.5
v_2^α	9.0	−12.4	10.8	−11.4	11.1	−11.2
t_1^{rev}	103	80	88	85	86	86
v_1^β	−9.9	−15.6	−13.7	−16.9	−15.5	−15.5
v_2^β	10.1	−13.8	12.4	−13.0	12.9	−12.9
v_1^σ	−9.7	−15.4	−13.7	−17.0	−15.8	−15.9
v_2^σ	10.2	−13.9	12.7	−13.3	13.3	−13.2

Table 3. Physical parameters of a light-fluid layer, where A_t and A_c denote the new modified Atwood numbers calculated with (3.7*a,b*); v_1^α (v_2^α) denotes the first (second) interface amplitude growth rate in stage α calculated with (3.6); t_1^{rev} denotes the end time of the first interface's phase reversal calculated with (3.8); v_1^β (v_2^β) denotes the first (second) interface amplitude growth rate in stage β calculated with (3.9*a,b*); and v_1^σ (v_2^σ) denotes the first (second) interface amplitude growth rate in stage σ calculated with (3.11*a,b*). The units for time and velocity are μs and m s^{-1}, respectively.

evaluated as

$$t_1^{rev} = Z_1 a_1^0 / |v_1^\alpha|, \tag{3.8}$$

and the values of t_1^{rev} in all cases are listed in table 3. On comparing t_1^{rev} with t_1^β in table 2, it can be found that $t_1^{rev} > t_1^\beta$ under $L_0 = 10$ and 30 mm conditions and $t_1^{rev} < t_1^\beta$ under $L_0 = 50$ mm conditions. Because of the baroclinic mechanism created by the misalignment of the density gradient ($\nabla \rho$) and the pressure gradient (∇p), the RF_2^α deposits vorticity with opposite direction to the one deposited by the IS on the first interface, as sketched in figure 9(*a*). On the contrary, the RF_2^α impacts the first interface after the first interface's phase reversal under $L_0 = 50$ mm conditions, depositing vorticity with the same direction as that deposited by the IS on the first interface, as sketched in figure 9(*b*). As a result, the RF_2^α leads to the first interface being more stable if $t_1^{rev} > t_1^\beta$, and being more unstable if $t_1^{rev} < t_1^\beta$. For the second interface, the RF_1^α induces vorticity deposition with the same direction as that deposited by the TS_1 on the second interface; therefore the RF_1^α certainly destabilises the second interface. Because the two interfaces evolve in the linear stage before the reflected waves (RF_2^α and RF_1^α) separately impact them, it is reasonable to adopt the re-shock impulsive theory proposed by Mikaelian (1985) (M model) to deduce the primary post-reshock amplitude growth rates as

$$v_1^\beta = v_1^\alpha + k a_1^\beta A(u_1^\beta - u_1^\alpha), \quad v_2^\beta = v_2^\alpha - k a_2^\beta A(u_2^\beta - u_2^\alpha), \tag{3.9a,b}$$

where a_1^β denotes the first interface amplitude at t_1^β and a_2^β denotes the second interface amplitude at t_2^β, and they are deduced as

$$a_1^\beta = Z_1 a_1^0 + v_1^\alpha t_1^\beta, \quad a_2^\beta = Z_2 a_2^0 + v_2^\alpha (t_2^\beta - t_2^\alpha). \tag{3.10a,b}$$

The values of v_1^β and v_2^β are listed in table 3. The predictions of the M model in stage β are shown with solid light purple lines for the first interface and dashed light purple lines for the second interface in figure 8 for all cases, and agree well with the experimental results.
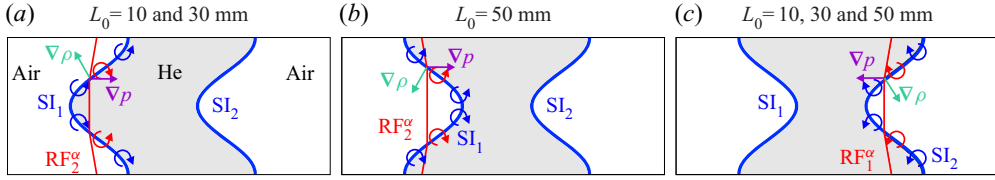
933 A10-12

Figure 9. Sketches of (*a*) the interaction of the RF_2^α and SI_1 under $L_0 = 10$ and 30 mm conditions, (*b*) the interaction of the RF_2^α and SI_1 under $L_0 = 50$ mm condition and (*c*) the interaction of RF_1^α and SI_2. The blue (red) arc with an arrow in (*a,b*) illustrates the vorticity deposition induced by the IS (RF_2^α) on the first interface. The blue (red) arc with an arrow in (*c*) illustrates the vorticity deposition induced by the TS_1 (RF_1^α) on the second interface. The purple (green) arrows represent the pressure (density) gradient ∇p ($\nabla \rho$).

In stage σ, the RF_2^β (RF_1^β) deposits additional vorticity on the first (second) interface, resulting in a secondary post-reshock amplitude growth rate, i.e. v_1^σ (v_2^σ), different from v_1^β (v_2^β). Because the condition that $t_1^{rev} > t_1^\beta$ is only satisfied in the two $L_0 = 10$ mm cases, the RF_2^β leads to the first interface being more stable under $L_0 = 10$ mm conditions, and being more unstable under $L_0 = 30$ and 50 mm conditions. Similar to stage β, the RF_1^β certainly destabilises the second interface. Here, we replace the primary post-reshock parameters in the M model with the secondary post-reshock parameters in stage σ to derive v_1^σ and v_2^σ as

$$v_1^\sigma = v_1^\beta + ka_1^\sigma A(u_1^\sigma - u_1^\beta), \quad v_2^\sigma = v_2^\beta - ka_2^\sigma A(u_2^\sigma - u_2^\beta), \tag{3.11a,b}$$

where a_1^σ denotes the first interface amplitude at t_1^σ and a_2^σ denotes the second interface amplitude at t_2^σ:

$$a_1^\sigma = a_1^\beta + v_1^\beta(t_1^\sigma - t_1^\beta), \quad a_2^\sigma = a_2^\beta + v_2^\beta(t_2^\sigma - t_2^\beta). \tag{3.12a,b}$$

The values of v_1^σ and v_2^σ are listed in table 3. The predictions of the M model in stage σ are shown with solid orange lines for the first interface and dashed orange lines for the second interface in figure 8 for all cases, and agree with the experimental results in early regimes. Due to the nonlinearity effect on the RMI (Velikovich & Dimonte 1996; Zhang & Sohn 1997; Nishihara *et al.* 2010), the amplitude growths of the two interfaces deviate from the M model predictions at a later time. Therefore, the nonlinearity effect on the RMI of a light-fluid layer should be considered in stage σ.

Here, we adopt the model of Dimonte & Ramaprabhu (2010) (DR model) by considering various amplitude-to-wavelength ratios and density ratios to quantify the nonlinearity effect. The expressions of the DR model for the first interface spike/bubble amplitude growth rate ($v_{1s/1b}$) and the second interface spike/bubble amplitude growth rate ($v_{2s/2b}$) are

$$\left. \begin{aligned} v_{ns/nb} &= \frac{v_n^\sigma \left[1 + (1 \mp A)k|v_n^\sigma|t\right]}{1 + C_{ns/nb}k|v_n^\sigma|t + (1 \mp A)F_{s/b}(k|v_n^\sigma|t)^2}, \\ C_{ns/nb} &= \frac{4.5 \pm A + (2 \mp A)k|a_n^\sigma|}{4}, \quad F_{s/b} = 1 \pm A, \end{aligned} \right\} \tag{3.13}$$

where $n = 1$ for the first interface and $n = 2$ for the second interface, and the upper (lower) sign of $\pm$ and $\mp$ in (3.13) applies to the spike (bubble). The DR model predictions for a_1 and a_2 are shown with solid green lines and dashed green lines, respectively, in figure 8

and agree well with all experimental results except for the L10-IP and L30-IP cases. The experimental growths of a_1 and a_2 in the two cases (the L10-IP and L30-IP cases) are lower than the DR model predictions, which can be ascribed to the collision of the two interfaces' spikes when the initial fluid layers are thin.

We regard that when the sum of the spike amplitudes of the two interfaces predicted by the DR model reaches the saturated layer thickness ($0.77L_0$) in cases L10-IP and L30-IP, $v_{1s} = 0$ and $v_{2s} = 0$. Then, the bubble amplitude growths of the two interfaces determine the instability developments. The predictions of the modified DR model (mDR model) for a_1 and a_2 in cases L10-IP and L30-IP are shown with solid dark purple lines and dashed dark purple lines in figures 8(a) and 8(c), respectively, and agree well with experimental results at a later time.

3.3. *Comparison between light-fluid layer and heavy-fluid layer*

Finally, the two interface amplitude growths under the light-fluid-layer and heavy-fluid-layer conditions (Liang & Luo 2021a) are compared, as shown in figure 10. The incident shock strength, initial layer thicknesses and amplitude combinations are the same, but the Atwood number is the opposite between the light-fluid-layer and heavy-fluid-layer cases.

(i) On comparing with light-fluid-layer cases, the heavy-fluid layer's first interface amplitude deviates from its second interface amplitude more evidently. The rarefaction waves inside a heavy-fluid layer induce the additional Rayleigh–Taylor instability (RTI) (Rayleigh 1883; Taylor 1950) and the decompression effect on the first interface, and the compression waves inside a heavy-fluid layer induce the additional Rayleigh–Taylor stabilisation (RTS) and the compression effect on the second interface (Liang & Luo 2021a). As a result, the two interface amplitude growths obviously deviate from each other. Since the reflected shocks reverberating inside a light-fluid layer are rather weak, the light-fluid layer's two interface amplitude growths are similar. Further, the first (second) interface amplitude growth rate in stage α under the light-fluid-layer condition, v_1^{light} (v_2^{light}), and that under the heavy-fluid-layer condition, v_1^{heavy} (v_2^{heavy}), are calculated according to (3.6) in this study and (3.9) in our previous work (Liang & Luo 2021a), respectively.

(ii) The ratio of v_1^{light} to v_1^{heavy} versus kL_0 is shown in figure 11(a). Because the jump velocity imposed by the IS on the light-fluid layer's first interface is larger than the heavy-fluid-layer counterpart, v_1^{light} is obviously larger than v_1^{heavy} especially if the two interfaces are initially in phase. However, due to the RTI and the decompression effect induced by the rarefaction waves on the heavy-fluid layer's first interface, the interface's instability is prominently enlarged, and, therefore, the late-time a_1 of a heavy-fluid layer is even greater than that of a light-fluid layer.

(iii) The ratio of v_2^{light} to v_2^{heavy} versus kL_0 is shown in figure 11(b). The jump velocities imposed by the TS$_1$ on the second interface of a light-fluid layer and a heavy-fluid layer are similar. Therefore, the difference between v_2^{light} and v_2^{heavy} is mainly ascribed to the interface-coupling effect. Despite v_2^{light} being larger than v_2^{heavy} if the two interfaces are initially in phase, v_2^{light} and v_2^{heavy} approach the same value when kL_0 is more extensive. If the two interfaces are initially anti-phase, $v_2^{light} < v_2^{heavy}$ when $kL_0 < 3.5$ and $v_2^{light} > v_2^{heavy}$ when $kL_0 > 3.5$. Except for case L10-AP, due to the RTS and the compression effect, a_2 under the heavy-fluid-layer condition is generally lower than that under the
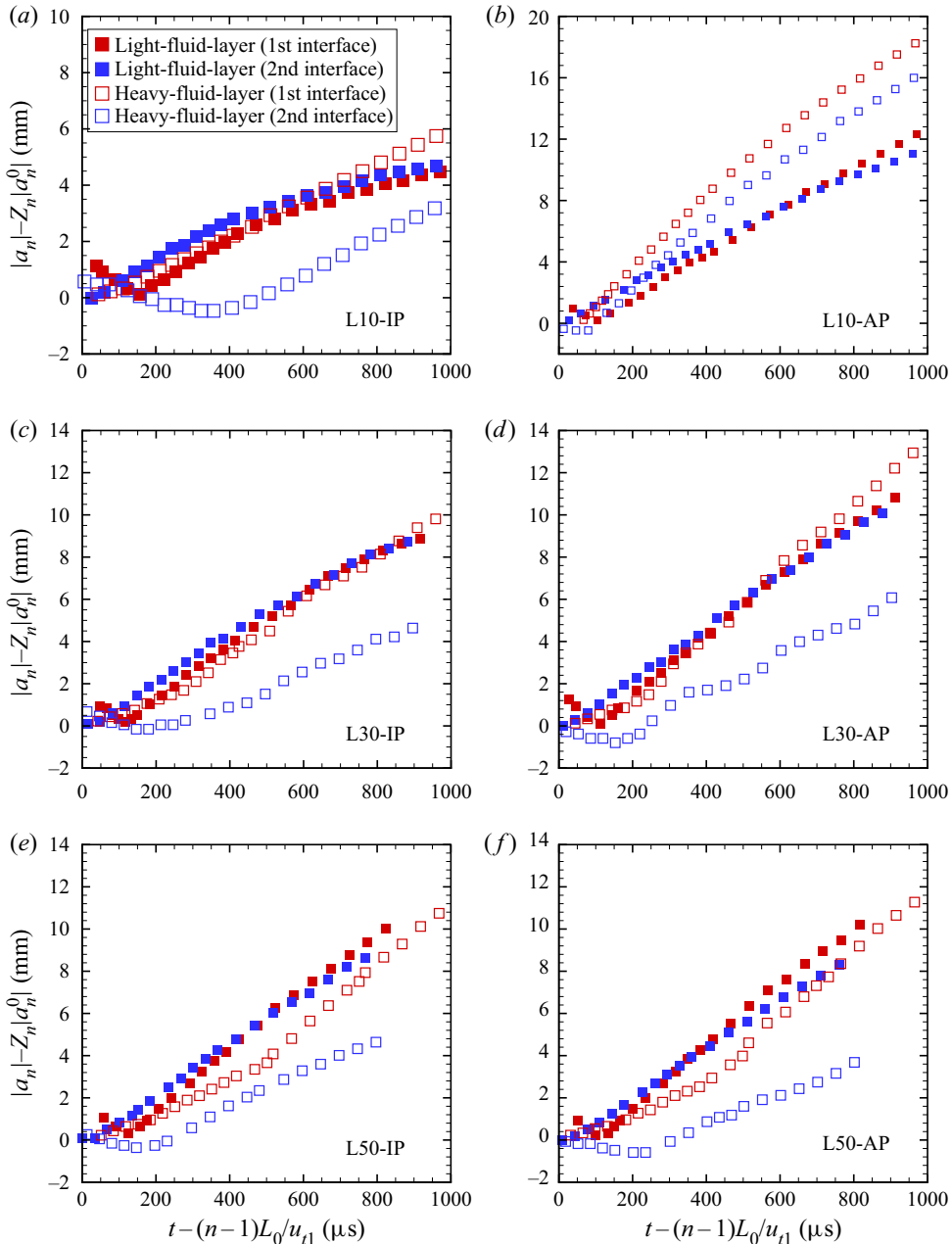
933 A10-14

Figure 10. Comparisons of the two interface amplitude growths under the light-fluid-layer condition and heavy-fluid-layer condition in cases (*a*) L10-IP, (*b*) L10-AP, (*c*) L30-IP, (*d*) L30-AP, (*e*) L50-IP and (*f*) L50-AP.

light-fluid-layer condition. In case L10-AP, the two interfaces of a heavy-fluid layer coincide. Therefore, the heavy-fluid layer's second interface is destabilised by the first interface counterpart (Liang & Luo 2021*a*), and a_2 is larger under the heavy-fluid-layer condition than under the light-fluid-layer condition.
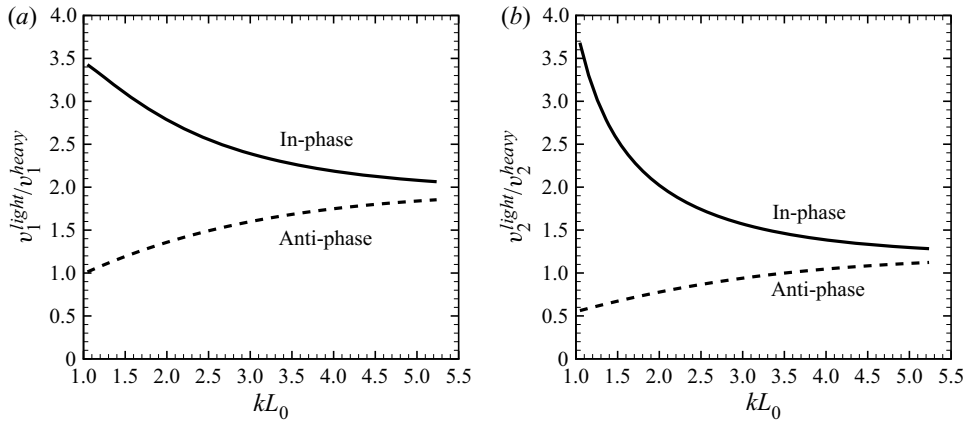
Figure 11. (*a*) The ratio of the first interface amplitude growth rate in stage α under the light-fluid-layer condition (v_1^{light}) to that under the heavy-fluid-layer condition (v_1^{heavy}) versus kL_0 and (*b*) the ratio of the second interface amplitude growth rate in stage α under the light-fluid-layer condition (v_2^{light}) to that under the heavy-fluid-layer condition (v_2^{heavy}) versus kL_0.

4. Conclusions

Shock-tube experiments on a finite-thickness helium gas layer are performed to investigate the wave patterns, interface motions and interfacial instabilities at both sides of the layer. The extended soap film technique is utilised to create three quasi-1-D fluid layers with different thicknesses and six quasi-2-D fluid layers with diverse thicknesses and amplitude combinations. Schlieren photography combined with a high-speed camera provides legible experimental pictures.

First, wave patterns and interface motions in the three quasi-1-D light-fluid-layer cases are studied. The reflected shocks inside a light-fluid layer decelerate the first interface but accelerate the second interface. After the second interface is accelerated by reflected shocks twice, it is reasonable to regard that all waves refract outside the fluid layer, and the two interfaces move at the same speed. Finally, the fluid-layer thickness reaches a saturated value of $0.77L_0$. A general 1-D theory is adopted to describe the two interfaces' motions and the layer thickness variations.

Second, the morphologies of a shocked quasi-2-D light-fluid layer are investigated. The final phases of the two interfaces are opposite when the two interfaces are initially in phase, while the final phases of the two interfaces are the same when the two interfaces are initially anti-phase. For the first time, it is observed that the two interfaces' spike heads collide when the two interfaces are in phase, and the initial fluid layer is very thin.

Third, the RMI development of a 2-D light-fluid layer is separated into three stages. Stage α: before multiple reflected shocks inside a light-fluid layer impact the first (second) interface, the vorticity induced by the incident shock (transmitted shock) and the interface-coupling effect dominate the first (second) interface perturbation growth. Stage β: if the end time of the first interface's phase reversal (i.e. t_1^{rev}) is smaller (larger) than the time when the primary reflected shock impacts the first interface (i.e. t_1^{β}), the primary reflected shock destabilises (stabilises) the first interface. The primary reflected shock results in the second interface being more unstable. Stage σ: if t_1^{rev} is smaller (larger) than the time when the secondary reflected shock impacts the first interface (i.e. t_1^{σ}), the

933 A10-16

secondary reflected shock also destabilises (stabilises) the first interface. The secondary reflected shock also results in the second interface being more unstable. Further, the nonlinearity effect suppresses the RMI of the two interfaces in stage σ.

Fourth, the linear amplitude growths of the two interfaces in stage α can be well described by the mJ model considering the interface-coupling effect and pre- and post-shock physical parameters. The linear amplitude growths of the two interfaces in stages β and σ can be well described by the re-shock impulsive theory considering the multiple reflected shocks reverberating inside a light-fluid layer. The nonlinearity effect on the RMI in stage σ can be characterised by the DR model. The restriction on the RMI due to the collision of the two interfaces' spike heads can be well described by the mDR model, regarding the two interface spike amplitude growth rates being identical to zero after the sum of the two interface spike amplitudes predicted by the DR model reaches the saturated layer thickness.

Fifth, the present study is the first to compare the two interface amplitude growths under the light-fluid-layer and heavy-fluid-layer conditions with the same incident shock intensity, initial layer thickness and amplitude combination, and the opposite Atwood number. It is concluded that the kind of waves reverberating inside a fluid layer significantly influences its evolution. The two interface amplitude growths under the light-fluid-layer condition are closer to each other than those under the heavy-fluid-layer condition. Although the mJ model predicts a larger amplitude growth rate of the light-fluid layer's first interface, the heavy-fluid layer's first interface amplitude is close to, or even greater than the light-fluid-layer counterpart, which is ascribed to the RTI and the decompression effect imposed by the rarefaction waves on the heavy-fluid layer's first interface. Due to the RTS and the compression effect imposed by the compression waves on the heavy-fluid layer's second interface, the heavy-fluid layer's second interface amplitude growth is generally smaller than the light-fluid-layer counterpart.

Declaration of interests. The authors report no conflict of interest.

Author ORCIDs.
Yu Liang https://orcid.org/0000-0002-3254-7073;
Xisheng Luo https://orcid.org/0000-0002-4303-8290.

REFERENCES

BALAKUMAR, B.J., ORLICZ, G.C., RISTORCELLI, J.R., BALASUBRAMANIAN, S., PRESTRIDGE, K.P. & TOMKINS, C.D. 2012 Turbulent mixing in a Richtmyer–Meshkov fluid layer after reshock: velocity and density statistics. *J. Fluid Mech.* **696**, 67–93.

BALAKUMAR, B.J., ORLICZ, G.C., TOMKINS, C.D. & PRESTRIDGE, K. 2008 Simultaneous particle-image velocimetry-planar laser-induced fluorescence measurements of Richtmyer–Meshkov instability growth in a gas curtain with and without reshock. *Phys. Fluids* **20**, 124103.

BROUILLETTE, M. 2002 The Richtmyer–Meshkov instability. *Annu. Rev. Fluid Mech.* **34**, 445–468.

BUDZINSKI, J.M., BENJAMIN, R.F. & JACOBS, J.W. 1994 Influence of initial conditions on the flow patters of a shock-accelerated thin fluid layer. *Phys. Fluids* **6**, 3510–3512.

DIMONTE, G. & RAMAPRABHU, P. 2010 Simulations and model of the nonlinear Richtmyer–Meshkov instability. *Phys. Fluids* **22**, 014104.

DING, J., LI, J., SUN, R., ZHAI, Z. & LUO, X. 2019 Convergent Richtmyer–Meshkov instability of a heavy gas layer with perturbed outer interface. *J. Fluid Mech.* **878**, 277–291.

DRAKE, R.P. 2018 *High-Energy-Density Physics: Foundation of Inertial Fusion and Experimental Astrophysics*. Springer.

HAINES, B.M., *et al.* 2021 Constraining computational modeling of indirect drive double shell capsule implosions using experiments. *Phys. Plasmas* **28** (3), 032709.

JACOBS, J.W., JENKINS, D.G., KLEIN, D.L. & BENJAMIN, R.F. 1995 Nonlinear growth of the shock-accelerated instability of a thin fluid layer. *J. Fluid Mech.* **295**, 23–42.

JACOBS, J.W., KLEIN, D.L., JENKINS, D.G. & BENJAMIN, R.F. 1993 Instability growth patterns of a shock-accelerated thin fluid layer. *Phys. Rev. Lett.* **70**, 583–586.

KURANZ, C.C., *et al.* 2018 How high energy fluxes may affect Rayleigh–Taylor instability growth in young supernova remnants. *Nat. Commun.* **9**, 1564.

LIANG, Y., LIU, L., ZHAI, Z., SI, T. & WEN, C.-Y. 2020 Evolution of shock-accelerated heavy gas layer. *J. Fluid Mech.* **886**, A7.

LIANG, Y. & LUO, X. 2021*a* On shock-induced heavy-fluid-layer evolution. *J. Fluid Mech.* **920**, A13.

LIANG, Y. & LUO, X. 2021*b* Shock-induced dual-layer evolution. *J. Fluid Mech.* **929**, R3.

LIANG, Y., ZHAI, Z., DING, J. & LUO, X. 2019 Richtmyer–Meshkov instability on a quasi-single-mode interface. *J. Fluid Mech.* **872**, 729–751.

LINDL, J., LANDEN, O., EDWARDS, J., MOSES, E. & TEAM, N. 2014 Review of the national ignition campaign 2009–2012. *Phys. Plasmas* **21**, 020501.

LIU, L., LIANG, Y., DING, J., LIU, N. & LUO, X. 2018 An elaborate experiment on the single-mode Richtmyer–Meshkov instability. *J. Fluid Mech.* **853**, R2.

LUO, X., LIANG, Y., SI, T. & ZHAI, Z. 2019 Effects of non-periodic portions of interface on Richtmyer–Meshkov instability. *J. Fluid Mech.* **861**, 309–327.

MESHKOV, E.E. 1969 Instability of the interface of two gases accelerated by a shock wave. *Fluid Dyn.* **4**, 101–104.

MEYER, K.A. & BLEWETT, P.J. 1972 Numerical investigation of the stability of a shock-accelerated interface between two fluids. *Phys. Fluids* **15**, 753–759.

MIKAELIAN, K.O. 1985 Richtmyer–Meshkov instabilities in stratified fluids. *Phys. Rev.* A **31**, 410–419.

MIKAELIAN, K.O. 1996 Numerical simulations of Richtmyer–Meshkov instabilities in finite-thickness fluid layers. *Phys. Fluids* **8** (5), 1269–1292.

MONTGOMERY, D.S., *et al.* 2018 Design considerations for indirectly driven double shell capsules. *Phys. Plasmas* **25** (9), 092706.

NISHIHARA, K., WOUCHUK, J.G., MATSUOKA, C., ISHIZAKI, R. & ZHAKHOVSKY, V.V. 2010 Richtmyer–Meshkov instability: theory of linear and nonlinear evolution. *Phil. Trans. R. Soc. Lond.* A **368**, 1769–1807.

OLMSTEAD, D., WAYNE, P., YOO, J.-H., KUMAR, S., TRUMAN, C.R. & VOROBIEFF, P. 2017 Experimental study of shock-accelerated inclined heavy gas cylinder. *Exp. Fluids* **58** (6), 71.

ORLICZ, G.C., BALAKUMAR, B.J., TOMKINS, C.D. & PRESTRIDGE, K.P. 2009 A Mach number study of the Richtmyer–Meshkov instability in a varicose, heavy-gas curtain. *Phys. Fluids* **21** (6), 064102.

ORLICZ, G.C., BALASUBRAMANIAN, S. & PRESTRIDGE, K.P. 2013 Incident shock Mach number effects on Richtmyer–Meshkov mixing in a heavy gas layer. *Phys. Fluids* **25** (11), 114101.

PRESTRIDGE, K., VOROBIEFF, P., RIGHTLEY, P.M. & BENJAMIN, R.F. 2000 Validation of an instability growth model using particle image velocimtery measurement. *Phys. Rev. Lett.* **84**, 4353–4356.

RAYLEIGH, LORD 1883 Investigation of the character of the equilibrium of an incompressible heavy fluid of variable density. *Proc. Lond. Math. Soc.* **14**, 170–177.

RICHTMYER, R.D. 1960 Taylor instability in shock acceleration of compressible fluids. *Commun. Pure Appl. Maths* **13**, 297–319.

RIGHTLEY, P.M., VOROBIEFF, P. & BENJAMIN, R.F. 1997 Evolution of a shock-accelerated thin fluid layer. *Phys. Fluids* **9** (6), 1770–1782.

ROMERO, B.E., POROSEVA, S., VOROBIEFF, P. & REISNER, J. 2021 Shock driven Kelvin–Helmholtz instability. *AIAA Scitech 2021 Forum*.

SUN, R., DING, J., ZHAI, Z., SI, T. & LUO, X. 2020 Convergent Richtmyer–Meshkov instability of heavy gas layer with perturbed inner surface. *J. Fluid Mech.* **902**, A3.

TAYLOR, G. 1950 The instability of liquid surfaces when accelerated in a direction perpendicular to their planes. I. *Proc. R. Soc. Lond.* A **201** (1065), 192–196.

TOMKINS, C., KUMAR, S., ORLICZ, G. & PRESTRIDGE, K. 2008 An experimental investigation of mixing mechanisms in shock-accelerated flow. *J. Fluid Mech.* **611**, 131–150.

TOMKINS, C.D., BALAKUMAR, B.J., ORLICZ, G., PRESTRIDGE, K.P. & RISTORCELLI, J.R. 2013 Evolution of the density self-correlation in developing Richtmyer–Meshkov turbulence. *J. Fluid Mech.* **735**, 288–306.

VELIKOVICH, A.L. & DIMONTE, G. 1996 Nonlinear perturbation theory of the incompressible Richtmyer–Meshkov instability. *Phys. Rev. Lett.* **76** (17), 3112.

ZHAI, Z., ZOU, L., WU, Q. & LUO, X. 2018 Review of experimental Richtmyer–Meshkov instability in shock tube: from simple to complex. *Proc. Inst. Mech. Engrs* **232**, 2830–2849.

ZHANG, Q. & SOHN, S.I. 1997 Nonlinear theory of unstable fluid mixing driven by shock wave. *Phys. Fluids* **9**, 1106–1124.

ZHOU, Y. 2017*a* Rayleigh–Taylor and Richtmyer–Meshkov instability induced flow, turbulence, and mixing. I. *Phys. Rep.* **720–722**, 1–136.

ZHOU, Y. 2017*b* Rayleigh–Taylor and Richtmyer–Meshkov instability induced flow, turbulence, and mixing. II. *Phys. Rep.* **723–725**, 1–160.